Research Square

Preprints are preliminary reports that have not undergone peer review.
They should not be considered conclusive, used to inform clinical practice,
or referenced by the media as validated information.

# Realization of a Tunable Two-dimensional Su-Schrieffer-Heeger Model in Monolayer $Mo_6Te_6$

**Vladislav Khaustov**

vladislav.khaustov@iit.it

Italian Institute of Technology https://orcid.org/0000-0001-6910-5511

**Giovanni Marini**

University of Trento https://orcid.org/0000-0003-2619-0925

**Janis Köster**

University of Ulm

**Michal Ochapski**

Italian Institute of Technology

**Zewdu M. Gebeyehu**

Istituto Italiano di Tecnologia

**Neeraj Mishra**

Italian Institute of Technology

**Stiven Forti**

Center for Nanotechnology Innovation IIT https://orcid.org/0000-0002-8939-3175

**Ute Kaiser**

University of Ulm https://orcid.org/0000-0003-0582-4044

**Matteo Calandra**

University of Trento https://orcid.org/0000-0003-1505-2535

**Camilla Coletti**

Italian Institute of Technology https://orcid.org/0000-0002-8134-7633

**Article**

**Keywords:**

**Posted Date:** June 4th, 2026

**DOI:** https://doi.org/10.21203/rs.3.rs-9909212/v1

**License:** This work is licensed under a Creative Commons Attribution 4.0 International License.
Read Full License

**Additional Declarations:** There is **NO** Competing Interest.

# Abstract

The two-dimensional Su-Schrieffer-Heeger (2D-SSH) model is a paradigmatic framework for understanding topological properties of matter. However, an experimental realization in an intrinsic material platform is still lacking, limiting the exploration of these phenomena in condensed matter systems. Here, we introduce 2D-$Mo_6Te_6$, a monolayer of self-assembled $Mo_6Te_6$ nanowires, as the first experimental realization of the 2D-SSH model in a free-standing material. 2D-$Mo_6Te_6$ features a variety of thermodynamically stable crystalline phases which are identified by high-resolution transmission electron microscopy (HRTEM) combined with density functional theory (DFT) simulations. The material is synthesized via scalable defect-mediated approach, and presents anisotropic optical properties as revealed by linearly polarized Raman spectroscopy. The existence of multiple metastable structural phases, combined with its chemical tunability, allows to explore the topological properties of the 2D-SSH model in great detail and opens to a plethora of applications in the field of topological condensed matter physics.


# 1. Introduction

Ever since the discovery of quantized Hall conductance, topological order has emerged as a fundamental paradigm in our understanding of phases of matter beyond the Landau-Ginzburg theory of phase transitions [1], [2], [3]]. In this context, the theoretical prediction [4] and experimental confirmation [5] of topological insulators represented a major breakthrough. One of the simplest realizations of topological order is the Su-Schrieffer-Heeger (SSH) model [6], a one-dimensional spinless tight-binding model originally introduced to describe solitons in polyacetylene. Depending on the ratio of intercell to intracell hopping, a zero-energy edge state may appear, protected by topology [7], [8].

Extensions of the SSH model into two-dimensions (2D-SSH) have been theoretically investigated in selected cases for their intriguing topological properties [9], [10]. In particular, a $C_4$-symmetric version of the 2D-SSH model has been proposed to host a novel topological insulator phase characterized by a different $\mathbb{Z}_2$ invariant compared to the Quantum Spin Hall insulator (QSHI) phase [9]. Despite this theoretical interest, the 2D-SSH model has been scarcely studied as it has not been realized in a real material until recently [11], when Geng *et al.* reported a lattice of Si atoms on Ag(001). However, in this structure, substrate interactions open a gap at the Dirac point, preventing a truly intrinsic realization.

In this work, we introduce two-dimensional molybdenum telluride (2D-$Mo_6Te_6$) as the first free-standing realization of a 2D-SSH system in a crystalline material and demonstrate its scalable synthesis. To date, 1D transition metal chalcogenide nanowires $M_6X_6$ (M = W, Mo; X = S, Se, Te) of nanometer-length have been synthesized by means of electron beam irradiation and/or ultra-high-vacuum (UHV) annealing of an initial $MX_2$ transition metal dichalcogenide (TMD) [12], [13], [14]. These nanowires exhibit remarkable mechanical and electronic properties in isolated 1D form [15], [16], [17]. First-principles calculations indicate that isolated $M_6X_6$ wires hold the potential to realize 1D topological states [18]. Indeed, $Mo_6Te_6$ nanowires have been obtained as isolated wires and also in the form of bundles, i.e., 3D-stacked wires,

via annealing and decomposition of parent $MoTe_2$ [19], [20], [21]. 2D films of $W_6Te_6$ and $Mo_6Se_6$, have been obtained via CVD [22] and electron beam exposure combined with thermal annealing [23], respectively, whereas molecular beam epitaxy (MBE) has been reported to yield ultrathin $Mo_6Te_6$ films, approaching monolayer thickness over nanometer-scale regions [13]. Indeed, the demonstration of 2D-$Mo_6Te_6$, i.e., self-assembled chains of nanowires periodically ordered in both planar directions for more than a few nanometers, has not been reported until now.

Here we demonstrate that 2D-$Mo_6Te_6$, extending over tens of micrometers, can be obtained via UHV annealing of graphene-encapsulated monolayer $MoTe_2$ grown by chemical vapor deposition (CVD). HRTEM reveals multiple crystalline phases of 2D-$Mo_6Te_6$ which perfectly match with theoretical predictions based on DFT simulations. We report unique Raman signatures to identify monolayer 2D-$Mo_6Te_6$, unveil its distinctive optical properties and introduce it as a novel platform both for the study of topological properties of the 2D-SSH model and of higher-order topological states.

## 2. Results and discussion

The electronic properties of the isolated $Mo_6Te_6$ nanowire are well described by an extended 1D-SSH model [6] with a six-atom basis [18]. The resulting electronic structure consists in an insulating state whose conduction bands are constituted by a hole-doped Dirac cone, in agreement with first principles calculations, and presents the same topological properties of the conventional two-atom SSH model. In the light of this observation, we use a hole-doped version of the simpler two-atom SSH model to describe the isolated nanowire. Since we are interested in the description of a 2D array of nanowires we extend the model to also include a second periodic dimension and inter-wire coupling. The proposed model consists in the following nearest neighbor Hamiltonian:

$$H = \sum_{ij} - t_x c^{\dagger}_{i+1,j} c_{i,j} - f\left(i,j\right) t_y c^{\dagger}_{i,j+1} c_{i,j}$$

1

,

where, the **x** direction represents the chain direction, while **y** is the other periodic direction. Thus, here $t_x$ and $t_y$ represent nearest-neighbor intra-chain and interchain hopping parameters, respectively, while *f(i, j)* is a function defined on the lattice sites and its values will depend on the specific structural phase we are considering. In Fig. 1 (a, d, g) we report 2D-SSH models, which are different flavors of the 2D-SSH model with specific parameter choices [9], [10], and corresponding electronic band structures (calculated by Eq. (1)) are shown in panels (b, e, h). It is particularly important and challenging to find a single material where small structural modifications allow for a description of the different topological 2D-SSH models.

In Fig. 1 (c, f, i), we define three 2D-$Mo_6Te_6$ candidates for 2D-SSH model: S1, S2 and P2 (see Supplementary Materials and Figure S1 for more details on the phases). The chemical picture behind the tight binding (TB) model (panels (a, d, g)) is illustrated in the crystal structure panels (c, f, i) with the shortest distance between Te atoms belonging to different nanowires. The TB model for S1 phase is characterized by a parallel hopping along the **y** direction (see panel (a)) and representing the hopping between Te atoms corresponding to different nanowires (see panel (c)). The situation is different for the S2 structure (see panel (d)), where the $t_y$ hoppings are staggered so as the shortest Te-Te distance between the neighboring wires (see panel (f)). P2 structure has no $t_y$ hoppings (see panels (g, i)), but all small variations of the different P phases' band structures can be recovered simply by adding a small $t_y$ hopping with some particular symmetry. The corresponding first-principles band structures are shown in Figure S2, S3 and well reproduce the most important features of the Mo(d)-derived conduction manifold bands of the structures under investigation (see DFT simulated bands comparison in Figure S4). 2D-$Mo_6Te_6$ phases host a pair of Dirac cones (albeit gapped by spin-orbit coupling (SOC)) whose position in the Brillouin zone is not fixed by symmetry (see Figures S2, S3). The only exception is the P4 phase (see Figure S2), it has a singular Dirac cone because it contains only one nanowire in the unit cell, while other phases have two nanowires per unit cell. Both the k-space position of the Dirac cones in the Γ-X and the energy separation of the flat bands in the X-K direction can be tuned by the hopping strength. Rigidly doped 2D-$Mo_6Te_6$ is a topological insulator when SOC is taken into account and it represents a potential platform to study the interplay between different topological orders. To the best of our knowledge, 2D-$Mo_6Te_6$ represents the first experimental realization of the 2D-SSH model in a real material. For this reason, it is worth analyzing its topological properties in detail (see Supplementary Materials and following text).

We now turn to the topological properties that emerge from its effective 2D SSH lattice. Different from other 2D-SSH models studied before [9], [10], the current 2D model has a close resemblance to its 1D counterpart. It can still be seen as a batch of loosely coupled 1D chains (indeed, realistically $t_y$ is always a small fraction of $t_x$ in the real system). We find a surprisingly rich physics, with the topological phase $\delta t_x < 0$ hosting 4n surface states, with n being the finite number of cells, absent in the trivial phase. In contrast to the isolated SSH chain, the nanoribbon is characterized by the presence of both non-dispersing edge state, a typical surface feature of graphene-like particle-hole symmetric systems [24], as well as high-order corner states. These results demonstrate that 2D-$Mo_6Te_6$ is a novel platform both for the study of the topological properties of the SSH model and of higher-order topological insulators.

Finally, we study the effect of the inclusion of SOC, with a focus on the S2 phase, adding to the Hamiltonian a term of the form:

$$H_{SOC} = \lambda_{SOC} \sum_{i,j} \sum_{\ll i',j' \gg} i\sigma_z \nu_{ij} c^{\dagger}_{i',j'} c_{i,j} + h.c.$$

2

,

where *h.c.* is the hermitian conjugate, $\lambda_{SOC}$ is the SOC strength, $\sigma_z$ is the third Pauli matrix acting on the spin subspace, the ≪≫ sum is extended to next to nearest neighbors and $v_{i,j}$ = 1 or -1 if the hopping is clockwise or anti-clockwise. This aspect is worth investigating since first principles calculations with the inclusion of SOC show a gap opening of ≈ 20 meV in correspondence to the Dirac point (Figure S3). The resulting band structure is depicted in Fig. 2 (a): with the inclusion of SOC, the system becomes insulating at the charge neutrality point. We investigate the topological properties of this insulating phase studying the hybrid Wannier center behavior as a function of $k_x$, which we display in Fig. 2 (b). The partner-switching behavior of the Wannier centers indicate a nontrivial value of the Kane-Mele invariant and, thus, a QSHI phase [25], [26]. To further confirm this finding, we also verified the existence of two pairs of counter-propagating helical edge states in a finite slab with $n_y$ = 25. The resulting band structure is reported in Fig. 2 (c). Interestingly, we find that one pair of edge states has zero velocity $v_D$, while the other disperses linearly. This remains true for a finite interval of $\delta t_x$ values. After a certain critical value of ≈ 0.07 eV all the edge states disperse linearly (see Fig. 2 (d)). We thus conclude that 2D-$Mo_6Te_6$ constitutes a candidate material to observe: (i) corner states related to higher-order topology in 2D, (ii) the Quantum spin Hall effect (QSHE), and, more generally, (iii) nontrivial topological insulating phases that have been predicted in the 2D-SSH model and yet unobserved in any material.

We now demonstrate that one of the candidates for the physical realization of the previously introduced tunable 2D-SSH model, i.e., the two-dimensional ordered arrays of $Mo_6Te_6$ nanowires (2D-$Mo_6Te_6$), can be realized experimentally. The synthesis of 2D-$Mo_6Te_6$ was achieved by subjecting graphene-encapsulated monolayer $MoTe_2$ – both 1H and 1T' – obtained via liquid precursors CVD [27], [28] to UHV thermal annealing at temperatures above 700°C (see Methods). Graphene encapsulation was found to be instrumental to limit uncontrolled Te sublimation during UHV annealing thus leading to the formation of 1D $Mo_6Te_6$ nanowires, that orderly self-assemble to form 2D-$Mo_6Te_6$. Graphene and hBN encapsulation has been shown in the past to be instrumental to protect $MoTe_2$ from oxidation [27], [28], or radiation damage during HRTEM measurements [29], [30] and to prevent formation of 1D-$Mo_6Te_6$ in layered 2H-$MoTe_2$ up to 850°C [29]. Identification of monolayer 2D-$Mo_6Te_6$ was performed by using HRTEM and Raman spectroscopy.

High-resolution transmission electron microscopy (HRTEM) was employed to investigate the atomic structure of the synthesized 2D-$Mo_6Te_6$. Imaging was performed using a Cc/Cs-corrected SALVE microscope operated at an acceleration voltage of 80 kV, enabling high-resolution imaging while minimizing beam-induced damage and chromatic aberration effects.

Figure 3 shows representative HRTEM analysis of graphene-encapsulated 1H-$MoTe_2$ after annealing at 800°C for 40 minutes. The images reveal several distinct periodic in-plane structures extending over nanometer-scale regions. Panels (a–c) display three different lattice-resolved configurations, which are consistent with the S1–S3 structural phases predicted by DFT. The experimental contrast is compared with projected ball-and-stick models overlaid on the images, highlighting the agreement between the observed periodicities and the proposed atomic arrangements. In panel (d), a line defect is observed

within the S3 phase, corresponding to a relative lattice shift of approximately half a unit cell along the nanowire direction. This defect can be interpreted as a local structural rearrangement, where a P2-like unit is embedded within the S3 matrix, as schematically illustrated in panel (e). Such defects indicate the presence of low-energy transformations between competing polymorphs. Panel (e) further shows a larger-area HRTEM image of a continuous 2D-$Mo_6Te_6$ region together with the corresponding fast Fourier transform (FFT). The FFT exhibits well-defined diffraction spots, indicating a high degree of crystallinity and long-range ordering. Contributions from the graphene encapsulation layer can be identified separately from those of the $Mo_6Te_6$ lattice. Panels (f–h) present the FFT patterns corresponding to the structures shown in panels (a–c). The distinct reciprocal-space features are consistent with the expected lattice symmetries and periodicities of the respective phases, providing additional support for their identification.

Overall, the HRTEM analysis demonstrates the formation of extended, polymorphic 2D-$Mo_6Te_6$ domains with well-defined periodic structures. This represents a significant improvement compared to previously reported $Mo_6Te_6$ bundles obtained by annealing of unprotected $MoTe_2$ [20], [31], which typically exhibit reduced structural coherence and limited long-range ordering. No significant structural evolution was observed during imaging in our experiment, indicating that the observed configurations are not induced by the electron beam.

In Fig. 4 (a), we report the Raman spectroscopy signature of 2D-$Mo_6Te_6$ (blue line) which is distinctively different from the spectrum of bulk $Mo_6Te_6$ (black line). The 2D-$Mo_6Te_6$ spectrum features two main Raman modes: 1) a first one at 156 $cm^{-1}$, specific for both monolayer and layered $Mo_6Te_6$ [20], [32], [33]; 2) a second one observed at 253 ± 5 $cm^{-1}$, which is blueshifted with respect to the layered $Mo_6Te_6$ mode observed at 245 $cm^{-1}$ [20], [32], [33]. We note that an important Raman feature of monolayer $Mo_6Te_6$ is a high intensity ratio between the higher and lower wavenumber Raman modes which is consistently found in the range between 2 and 5. Previously, it was reported to be ~ 1 for 2–3 nm flakes thickness that correspond to 2–3 layers of $Mo_6Te_6$, [34]. The reported Raman modes are significantly different from those measured for monolayer 1H- and 1T'-$MoTe_2$ phases (see Figure S11), and exhibit positions variation among the samples (see Figure S12 for Raman spectra of 2D-$Mo_6Te_6$ obtained from different starting phases). The variability retrieved in the 253 $cm^{-1}$ mode position is assigned to the presence of the different phases observed for $Mo_6Te_6$.

We now present Raman mapping results which do not only allow us to discuss the mechanism behind the formation of 2D-$Mo_6Te_6$ but also provide demonstration of its scalable synthesis. $MoTe_2$ to $Mo_6Te_6$ polymorphism initiates where graphene, which is used for $MoTe_2$ oxidation protection, presents defects. The transition proceeds via material degradation, i.e., simultaneous Te atoms volatilization and Mo atoms in-plane diffusion similar to what was demonstrated in HRTEM experiments for different S and Se based TMDs [23]. This is clearly observed in Fig. 4 (b, c), where $Mo_6Te_6$ stripes – as confirmed by the Raman mapping analyses reported in panels (d, e) – appear underneath graphene wrinkles after

annealing $MoTe_2$ at 700°C for 60 minutes. These wrinkles, which are visible under optical microscopy, are confirmed by KPFM, AFM, and Raman analyses (see Figure S13). The $MoTe_2$ to $Mo_6Te_6$ transformation nucleates at these wrinkles and extends laterally for ~ 1µm each side, perpendicular to the wrinkle propagation direction.

Figure 4 (f) shows that graphene-encapsulated 1T'-$MoTe_2$ can be converted into continuous 2D-$Mo_6Te_6$ through controlled UHV annealing. Nucleation begins after 20 minutes at 800°C and expands with continued annealing. Since 1T'-$MoTe_2$ concurrently transforms into both 1H-$MoTe_2$ and $Mo_6Te_6$ at similar rates [30], distinguishing these phases is crucial. After 125 minutes, a nearly complete monolayer 2D-$Mo_6Te_6$ forms, with only minor traces of 1H- and 1T' phases remaining (see Fig. 4 (h)). Figure 4 (g) presents the phase evolution over time, highlighting both the 1T' to 1H transition and Te volatilization, the latter driving $Mo_6Te_6$ formation as the dominant phase after 60 minutes. Figures S14-S17 shows summarized data on the evolution of the graphene Raman modes after annealing. From the analysis of the annealing-dependent evolution of these modes, the following observations can be made: The D mode, initially localized at the wrinkles (see Figure S13), becomes more widespread after annealing at 800°C, indicating that while the $MoTe_2$-to-$Mo_6Te_6$ phase transition nucleates at 700°C beneath the wrinkles, at 800°C the transition is driven by a more general degradation of the graphene layer. Moreover, a significant difference in the 2D mode position after annealing at 800°C is observed when comparing graphene on $MoTe_2$ and graphene on $Mo_6Te_6$. In the latter case, the 2D mode position is comparable to that of annealed graphene on $SiO_2$. This suggests a release of graphene strain upon the transformation of $MoTe_2$ into $Mo_6Te_6$, whereas graphene on $MoTe_2$ remains under compressive strain.

A detailed linearly polarized Raman spectroscopy data, Raman tensor analysis, symmetry-resolved selection rules, and phonon mode assignment based on first-principles calculations are reported in the Supplementary Materials. Our findings indicate Resonant nature of the Raman response as well as anisotropic nature of the 2D-$Mo_6Te_6$ unit cell and confirm µm-scale crystallinity of the synthesized material. The strongest modes reach their maximum intensity when the incident light polarization is aligned parallel to the elongated seed of the initial 1T' flake. This optical anisotropy, reminiscent of that in 1T'-$MoTe_2$, where the seed typically elongates along the zig-zag direction [28], [35], [36], is consistent with the crystal point groups (see Table S1). This feature can be reliably used for identifying the principal crystallographic axis of 2D-$Mo_6Te_6$, instrumental for device fabrication and anisotropic transport measurements.

# 3. Conclusion

This work introduces monolayer 2D-$Mo_6Te_6$ as the first experimental realization of the 2D-SSH model in a free-standing crystalline material. The lateral assembly of $Mo_6Te_6$ nanowires gives rise to a family of two-dimensional phases that can be naturally mapped onto distinct 2D-SSH lattice models, providing a unique solid-state platform to explore topological phenomena beyond the one-dimensional SSH paradigm. Upon inclusion of spin-orbit coupling, the resulting electronic structure evolves into a quantum

spin Hall insulating phase, establishing 2D-$Mo_6Te_6$ as a versatile platform for the investigation of QSHE and higher-order topological phenomena.

Using a scalable defect-mediated synthesis approach, we demonstrate the transformation from monolayer $MoTe_2$ (both 1H and 1T') to monolayer 2D-$Mo_6Te_6$ at the mesoscale level and experimentally identify multiple planar stacking configurations, supported by first-principles calculations predicting additional metastable phases. The small energy differences between these phases, combined with their lattice mismatch, suggest promising opportunities for phase-selective synthesis through substrate engineering or strain control. In addition, the pronounced optical anisotropy and distinct Raman fingerprints provide practical routes for phase identification and crystallographic orientation in future device architectures.

More broadly, the combination of polymorphism, chemical tunability, and scalable synthesis establishes 2D-$Mo_6Te_6$ as a promising platform for exploring topological condensed matter physics. Extension of this strategy toward multilayer and three-dimensional architectures may further enable the realization of exotic topological phases within generalized 3D-SSH frameworks.

# 5. Methods

### 5.1. Growth of monolayer $MoTe_2$ using Liquid-Precursor Chemical Vapor Deposition

The $MoTe_2$ samples were grown via liquid precursor CVD on 285 nm thick $SiO_2$ on Si, as we previously reported in Pace et al. [27]. In this method, the molybdenum precursor is obtained from an aqueous solution and directly spun on the $SiO_2$ substrate. First, three mother solutions were prepared, namely, solutions A, B, and C. Solution A was obtained by dissolving 0.11 g of ammonium hepta-molybdate (AHM, Sigma-Aldrich), weighted by analytical balance ABJ 80-4NM, in 40 mL of DI water. Solution B was obtained by dissolving 0.1 g of NaOH (Sigma-Aldrich) in 40 mL of DI water. Solution C consists of OptiPrep (Sigma-Aldrich) used as purchased. The growth solution was obtained by mixing the mother solutions with the volume ratio A:B:C = 0.8:0.5:0.3. The growth solution was then spin-coated on a clean $SiO_2$/Si substrate at 300 rpm for 10 seconds, plus 20 seconds at 3000 rpm. Before spin-coating, all $SiO_2$ substrates were sonicated in acetone and isopropanol for 5 min and subsequently treated with oxygen plasma (power 100 W, process pressure 80 mTorr) for 5 min to increase the hydrophilicity of the $SiO_2$ surface. The spin-coated substrate and the metallic tellurium were then loaded in a Lenton hot-wall horizontal CVD reactor. The growth was carried out at near-atmospheric pressure for 3 min, under constant flow of Ar/$H_2$ ($H_2$ 3%) gas at 100 sccm. Best results were obtained at a growth temperature of 730 °C, with increased molybdenum precursor concentration, and by opening the CVD reactor at 700 °C. The duration of the growth process lasts for 3 minutes. After the growth, the reactor was allowed to cool rapidly under constant flux of Ar by opening the lid at 700 °C.

### 5.2. Semidry Encapsulation Method

Semidry encapsulation of as-grown $MoTe_2$ was obtained via delamination of graphene films grown on copper foil (Alfa-Aesar). Graphene samples were grown in-house using a 4” Aixtron BM Pro CVD reactor [37]. The graphene on foil was cut in squares of dimensions larger than the target $SiO_2$ sample. Then, it was covered with a double-layer polymeric membrane of PMMA AR-P 679.45 (Allresist) and 15% PPC in anisole (Sigma-Aldrich) by spin coating for 60 seconds at 2000 rpm and baked at 90 °C for 2 minutes. A PDMS supporting frame (few-millimeters thick) was placed on top of the sample. The sample was then floated in a NaOH electrolyte solution (1 M), where an electrochemical reaction takes place [37]: here the graphene on copper foil acts as anode and a platinum foil is used as cathode. A constant 2.42 V voltage was applied to the Pt electrode until the electrochemical delamination process was completed. The PPC/PMMA/graphene membrane was then left in DI water for 3 minutes to remove the NaOH residuals and then left to dry under the hood for 10-20 minutes to evaporate residual water from graphene surface.  After complete dry of the membrane, it was laminated on top of the as-grown $MoTe_2$ sample and heated at 90 °C for several minutes until the substrate is completely covered with graphene membrane. Finally, acetone was used to remove the supporting polymer, followed by isopropanol rinse.

### 5.3. Realization of graphene/$MoTe_2$/graphene and transfer on TEM grids

Graphene-encapsulated $MoTe_2$ was transferred using 1 M NaOH (Sigma-Aldrich) water solution. In particular, the sample was covered with a layer of 672.045 PMMA (Allresist), 15% PPC in anisole (Sigma-Aldrich) layer and PDMS frame, which was sequentially spun (60 seconds, 2000 rpm) and baked (90 °C. 2 min). Then, the sample was left floating in NaOH water solution until the complete detachment of the membrane. After detachment, the floating membrane was fished and rinsed in DI water for 4 minutes to minimize the exposure of $MoTe_2$ to oxidizing agents and dried under the hood for approximately 20 minutes. Finally, the PPC/PMMA/graphene/$MoTe_2$ membrane was placed on top of a $SiO_2$ substrate where CVD graphene was previously transferred and baked at 90 °C for few minutes. The polymeric membrane was then removed via a standard cleaning in acetone. The samples were then inserted in UHV and annealed. After UHV thermal annealing, the transfer procedure was repeated to transfer graphene/$MoTe_2$ ($Mo_6Te_6$)/graphene sandwiches on top of PVA/$SiO_2$ and then on TEM grids as described in [28]. In brief, optical microscopy was used to identify suitable graphene/$MoTe_2$/graphene structures on a VA/$SiO_2$ substrate with 285 nm $SiO_2$ thickness. Such flakes were then transferred to a Quantifoil R 1.2/1.3 TEM grid with the help of a drop of isopropyl alcohol (IPA) to bring the grid in contact with the flake. Evaporation of the IPA attached the grid to the flake. With water the underlying PVA was dissolved away, releasing the grid with the graphene/$MoTe_2$/graphene samples.

### 5.4. Characterization Techniques

The optical images of the samples were obtained with a microscope ZEISS Axioscope 7. Raman characterization was carried out with a Renishaw InVia spectrometer. The laser wavelength used were 473, 532 and 785 nm with a 100× lens and 0.85 NA in long exposure time mode (30-60/180 seconds) and low power (1.16/0.58 mW), and in short exposure time (1-2 seconds) and high power (5.8 mW)

mode. Polarized Raman measurements were implemented in $z(x,-)\bar{z}$ (H-), $z(x,y)\bar{z}$ (HV) and $z(y,y)\bar{z}$ (VV) configurations.

HRTEM imaging was carried out using a Cc/Cs-corrected SALVE microscope [38] operated at an acceleration voltage of 80 kV. The use of combined chromatic and spherical aberration correction enables high-resolution imaging at low accelerating voltages, which is essential to minimize beam-induced damage in beam-sensitive materials such as transition metal dichalcogenides. Images were acquired under phase-contrast conditions close to the Scherzer defocus, allowing reliable visualization of the projected atomic structure. The electron dose was kept as low as reasonably achievable in order to reduce beam-induced structural modifications during imaging. No significant structural evolution was observed under the applied imaging conditions. The vacuum pressure in the TEM column was on the order of $10^{-5}$ Pa. The chromatic and spherical aberration coefficients (Cc and Cs) were tuned in the range of −10 µm to −20 µm. Structural analysis was performed by comparing the experimental HRTEM images with projected atomic models derived from DFT. FFT analysis was used to extract reciprocal-space information and to assess lattice periodicity and symmetry.

Amplitude-modulated Kelvin Probe Force Microscopy (KPFM) was performed with a Bruker Dimension Icon microscope equipped with an FMV-PT probe without applying bias to the tip.

### 5.5. UHV thermal annealing

Thermal annealing was performed in a UHV chamber with the pressure not exceeding $10^{-8}$ mbar during the process. We performed a UHV thermal annealing using graphene/$MoTe_2$/$SiO_2$/Si and graphene/$MoTe_2$/graphene/$SiO_2$/Si configurations, and SiC substrate played the role of the resistive heater [30]. The temperature was measured using an IMPAC IGAR 6 pyrometer in a smart mode (emissivity independent).

### 5.6. Computational details

DFT calculations were performed with the open-source QE package [39], [40], [41]. The PAW method was used in the calculations [42] and the exchange-correlation functional was described by the PBE version of the GGA [43], [44]. The kinetic energy cutoffs for wavefunctions and charge density were set to 65 and 600 Ry, respectively. For simulations with SOC included, the kinetic energy cutoffs were set to 45 and 340 Ry, respectively. We used Marzari-Vanderbilt-Devita-Payne cold smearing approach for electronic occupations with 0.018 eV [45]. 12x4x1 and 12x6x1 wave-vector grids were used for 2D-$Mo_6Te_6$ unit cells and a vacuum spacing of at least 19 Å was introduced to avoid replicas interaction. The van der Waals interaction was based on the semiempirical dispersion-correction DFT-D3 method of Grimme [46]. The phonons were calculated using Trouiller-Martins-type local-density LDA norm-conserving pseudopotentials [47], [48] with 120 Ry kinetic energy cutoff for wavefunctions and 0.018 eV Marzari-Vanderbilt-Devita-Payne cold smearing for electronic occupations [45]. The non-resonant Raman spectrum of the 1D-$Mo_6Te_6$ was simulated by density functional perturbation theory implemented

withing QE package [49]. Point groups were determined within the QE package and angle-dependent Raman tensor analysis for Raman-active modes was performed within the online tool of the Bilbao Crystallographic Server [50], [51], [52], [53], [54].

All the TB calculations to study the topological properties of the 2D-SSH model here presented were performed employing Python Tight Binding (PythTB) package [55].

Ball-and-stick models of the structures, simulated within the QE package, were visualized with the XCrySDen software [56]. The visualization of the phonon modes was implemented by using online tool “Interactive phonon visualizer”.

## Declarations

# Acknowledgements

This work has received funding from the European Union's Horizon 2020 research and innovation programme under grant agreement 881603. We acknowledge financial support from NPRR MUR project PE000023-NQSTI funded by the European Union – NextGenerationEU. This research is funded by the Deutsche Forschungsgemeinschaft (DFG, German Research Foundation), No. 471707562. Funded by the European Union, Next Generation EU, mission4, component2, CUP E63C22000970007. We acknowledge EUROHPC (EHPC-REG-2024R01-06), for the availability of high performance computing resources and support. We gratefully acknowledge the Data Science and Computation Facility and its Support Team for their support and assistance on the IIT High Performance Computing Infrastructure.

## References

1. Thouless DJ, Kohmoto M, Nightingale MP, Nijs Mden (1982) Quantized Hall Conductance in a Two-Dimensional Periodic Potential, *Phys. Rev. Lett.*, vol. 49, no. 6, pp. 405–408, Aug. 10.1103/PhysRevLett.49.405
2. Qi X-L, Zhang S-C (2011) Topological insulators and superconductors, *Rev. Mod. Phys.*, vol. 83, no. 4, pp. 1057–1110, Oct. 10.1103/RevModPhys.83.1057
3. Hasan MZ, Kane CL (2010) Colloquium: Topological insulators, *Rev. Mod. Phys.*, vol. 82, no. 4, pp. 3045–3067, Nov. 10.1103/RevModPhys.82.3045
4. Kane CL, Mele EJ (Sep. 2005) ${Z}_{2}$ Topological Order and the Quantum Spin Hall Effect. Phys Rev Lett 95:146802. 10.1103/PhysRevLett.95.146802
5. König M et al (2007) Quantum Spin Hall Insulator State in HgTe Quantum Wells, *Science*, vol. 318, no. 5851, pp. 766–770, Nov. 10.1126/science.1148047
6. Su WP, Schrieffer JR, Heeger AJ (1979) Solitons in Polyacetylene, *Phys. Rev. Lett.*, vol. 42, no. 25, pp. 1698–1701, Jun. 10.1103/PhysRevLett.42.1698

7. Zak J (1989) Berry's phase for energy bands in solids, *Phys. Rev. Lett.*, vol. 62, no. 23, pp. 2747–2750, Jun. 10.1103/PhysRevLett.62.2747
8. Cayssol J, Fuchs JN (Apr. 2021) Topological and geometrical aspects of band theory. J Phys Mater 4(3):034007. 10.1088/2515-7639/abf0b5
9. Liu F, Wakabayashi K (Feb. 2017) Novel Topological Phase with a Zero Berry Curvature. Phys Rev Lett 118(7):076803. 10.1103/PhysRevLett.118.076803
10. Li C-A (Mar. 2022) Topological States in Two-Dimensional Su-Schrieffer-Heeger Models. Front Phys 10. 10.3389/fphy.2022.861242
11. Geng D et al (Nov. 2022) Observation of gapped Dirac cones in a two-dimensional Su-Schrieffer-Heeger lattice. Nat Commun 13(1):7000. 10.1038/s41467-022-34043-9
12. Lehtinen O et al (Mar. 2015) Atomic Scale Microstructure and Properties of Se-Deficient Two-Dimensional MoSe2. ACS Nano 9(3):3274–3283. 10.1021/acsnano.5b00410
13. Yu Y, Wang G, Tan Y, Wu N, Zhang X-A, Qin S (Feb. 2018) Phase-Controlled Growth of One-Dimensional Mo6Te6 Nanowires and Two-Dimensional MoTe2 Ultrathin Films Heterostructures. Nano Lett 18(2):675–681. 10.1021/acs.nanolett.7b03058
14. Yang X et al (Sep. 2020) Possible Phason-Polaron Effect on Purely One-Dimensional Charge Order of ${\mathrm{Mo}}_{6}{\mathrm{Se}}_{6}$ Nanowires. Phys Rev X 10(3):031061. 10.1103/PhysRevX.10.031061
15. Lin J et al (2014) Flexible metallic nanowires with self-adaptive contacts to semiconducting transition-metal dichalcogenide monolayers, *Nat. Nanotechnol.*, vol. 9, no. 6, Art. no. 6, Jun. 10.1038/nnano.2014.81
16. Lin J, Zhang Y, Zhou W, Pantelides ST (Feb. 2016) Structural Flexibility and Alloying in Ultrathin Transition-Metal Chalcogenide Nanowires. ACS Nano 10(2):2782–2790. 10.1021/acsnano.5b07888
17. Nagata M et al (Aug. 2019) Isolation of Single-Wired Transition-Metal Monochalcogenides by Carbon Nanotubes. Nano Lett 19(8):4845–4851. 10.1021/acs.nanolett.8b05074
18. Jin K-H, Liu F (2020) 1D topological phases in transition-metal monochalcogenide nanowires, *Nanoscale*, vol. 12, no. 27, pp. 14661–14667, Jul. 10.1039/D0NR03529G
19. Zhu H et al Defects and Surface Structural Stability of MoTe2 Under Vacuum Annealing, p. 13
20. Zhu H et al (2017) New Mo6Te6 Sub-Nanometer-Diameter Nanowire Phase from 2H-MoTe2. Adv Mater 29:1606264. 10.1002/adma.201606264
21. Yang Q et al (Jul. 2024) Constrained patterning of orientated metal chalcogenide nanowires and their growth mechanism. Nat Commun 15(1):6074. 10.1038/s41467-024-50525-4
22. Lim HE et al (Jan. 2021) Wafer-Scale Growth of One-Dimensional Transition-Metal Telluride Nanowires. Nano Lett 21(1):243–249. 10.1021/acs.nanolett.0c03456
23. Hong J et al (May 2022) Multiple 2D Phase Transformations in Monolayer Transition Metal Chalcogenides. Adv Mater 34(19):2200643. 10.1002/adma.202200643

24. Ryu S, Hatsugai Y (Jul. 2002) Topological Origin of Zero-Energy Edge States in Particle-Hole Symmetric Systems. Phys Rev Lett 89:077002. 10.1103/PhysRevLett.89.077002
25. Soluyanov AA, Vanderbilt D (2011) Computing topological invariants without inversion symmetry, *Phys. Rev. B*, vol. 83, no. 23, p. 235401, Jun. 10.1103/PhysRevB.83.235401
26. Yu R, Qi XL, Bernevig A, Fang Z, Dai X (Aug. 2011) Equivalent expression of ${\mathbb{Z}}_{2}$ topological invariant for band insulators using the non-Abelian Berry connection. Phys Rev B 84(7):075119. 10.1103/PhysRevB.84.075119
27. Pace S et al (2021) Synthesis of Large-Scale Monolayer 1T'-MoTe2 and Its Stabilization via Scalable hBN Encapsulation, *ACS Nano*, vol. 15, no. 3, pp. 4213–4225, Mar. 10.1021/acsnano.0c05936
28. Khaustov VO et al (Jul. 2023) Heterocontact-Triggered 1H to 1T' Phase Transition in CVD-Grown Monolayer MoTe2: Implications for Low Contact Resistance Electronic Devices. ACS Appl Nano Mater. 10.1021/acsanm.3c01314
29. Köster J et al (Jan. 2024) Phase transformations in single-layer MoTe2 stimulated by electron irradiation and annealing. Nanotechnology 35(14):145301. 10.1088/1361-6528/ad15bb
30. Khaustov VO et al (2025) Reversible semimetal–semiconductor phase transition in CVD-grown monolayer MoTe2, *2D Mater.*, vol. 12, no. 2, p. 025025, Mar. 10.1088/2053-1583/adbcc0
31. Li Y, Wu D, Wang D, Zhang Y, Min T, Pan Y (2023) Atomic-Scale Observation of the Local Structure and 1D Quantum Effects in vdW Stacking Mo6Te6 Nanowires. Adv Mater Interfaces 10(6):2202043. 10.1002/admi.202202043
32. Köster J et al (2021) Defect Agglomeration and Electron-Beam-Induced Local-Phase Transformations in Single-Layer MoTe $_2$, *J. Phys. Chem. C*, vol. 125, no. 24, pp. 13601–13609, Jun. 10.1021/acs.jpcc.1c02202
33. Kim H, Johns JE, Yoo Y (2020) Mixed-Dimensional In-Plane Heterostructures from 1D Mo6Te6 and 2D MoTe2 Synthesized by Te-Flux-Controlled Chemical Vapor Deposition. Small 16(47):2002849. 10.1002/smll.202002849
34. Empante TA et al (Jan. 2017) Chemical Vapor Deposition Growth of Few-Layer MoTe2 in the 2H, 1T', and 1T Phases: Tunable Properties of MoTe2 Films. ACS Nano 11(1):900–905. 10.1021/acsnano.6b07499
35. Chen S-Y, Naylor CH, Goldstein T, Johnson ATC, Yan J (Jan. 2017) Intrinsic Phonon Bands in High-Quality Monolayer T' Molybdenum Ditelluride. ACS Nano 11(1):814–820. 10.1021/acsnano.6b07260
36. Song Q et al (2017) Anomalous in-plane anisotropic Raman response of monoclinic semimetal 1 T´-MoTe 2, *Sci. Rep.*, vol. 7, no. 1, Art. no. 1, May 10.1038/s41598-017-01874-2
37. Miseikis V et al (2017) Deterministic patterned growth of high-mobility large-crystal graphene: a path towards wafer scale integration, *2D Mater.*, vol. 4, no. 2, p. 021004, Jan. 10.1088/2053-1583/aa5481
38. Linck M et al (Aug. 2016) Chromatic Aberration Correction for Atomic Resolution TEM Imaging from 20 to 80 kV. Phys Rev Lett 117:076101. 10.1103/PhysRevLett.117.076101

39. Giannozzi P et al (Sep. 2009) QUANTUM ESPRESSO: a modular and open-source software project for quantum simulations of materials. J Phys Condens Matter 21:395502. 10.1088/0953-8984/21/39/395502
40. Giannozzi P et al (Oct. 2017) Advanced capabilities for materials modelling with Quantum ESPRESSO. J Phys Condens Matter 29(46):465901. 10.1088/1361-648X/aa8f79
41. Giannozzi P et al (Apr. 2020) Quantum ESPRESSO toward the exascale. J Chem Phys 152:154105. 10.1063/5.0005082
42. Blöchl PE (1994) Projector augmented-wave method, *Phys. Rev. B*, vol. 50, no. 24, pp. 17953–17979, Dec. 10.1103/PhysRevB.50.17953
43. Prandini G, Marrazzo A, Castelli IE, Mounet N, Marzari N (2018) Precision and efficiency in solid-state pseudopotential calculations, *Npj Comput. Mater.*, vol. 4, no. 1, Art. no. 1, Dec. 10.1038/s41524-018-0127-2
44. Garrity KF, Bennett JW, Rabe KM, Vanderbilt D (Jan. 2014) Pseudopotentials for high-throughput DFT calculations. Comput Mater Sci 81:446–452. 10.1016/j.commatsci.2013.08.053
45. Marzari N, Vanderbilt D, De Vita A, Payne MC (Apr. 1999) Thermal Contraction and Disordering of the Al(110) Surface. Phys Rev Lett 82(16):3296–3299. 10.1103/PhysRevLett.82.3296
46. Grimme S, Antony J, Ehrlich S, Krieg H (Apr. 2010) A consistent and accurate ab initio parametrization of density functional dispersion correction (DFT-D) for the 94 elements H-Pu. J Chem Phys 132(15):154104. 10.1063/1.3382344
47. Troullier N, Martins JL (Jan. 1991) Efficient pseudopotentials for plane-wave calculations. Phys Rev B 43(3):1993–2006. 10.1103/PhysRevB.43.1993
48. Perdew JP, Wang Y (1992) Accurate and simple analytic representation of the electron-gas correlation energy, *Phys. Rev. B*, vol. 45, no. 23, pp. 13244–13249, Jun. 10.1103/PhysRevB.45.13244
49. Lazzeri M, Mauri F (Jan. 2003) First-Principles Calculation of Vibrational Raman Spectra in Large Systems: Signature of Small Rings in Crystalline S i O 2. Phys Rev Lett 90(3):036401. 10.1103/PhysRevLett.90.036401
50. I AM (2011) Crystallography online: Bilbao Crystallographic Server. Bulg Chem Commun 43:183–197
51. Aroyo MI et al (Jan. 2006) Bilbao Crystallographic Server: I. Databases and crystallographic computing programs. Z Für Krist - Cryst Mater 221(1):15–27. 10.1524/zkri.2006.221.1.15
52. Aroyo MI, Kirov A, Capillas C, Perez-Mato JM, Wondratschek H (2006) Bilbao Crystallographic Server. II. Representations of crystallographic point groups and space groups. Acta Crystallogr Sect A 62(2):115–128. 10.1107/S0108767305040286
53. Gallego SV, Etxebarria J, Elcoro L, Tasci ES, Perez-Mato JM (2019) Automatic calculation of symmetry-adapted tensors in magnetic and non-magnetic materials: a new tool of the Bilbao Crystallographic Server. Acta Crystallogr Sect A 75(3):438–447. 10.1107/S2053273319001748

54. Denisov VN, Mavrin BN, Podobedov VB (Jul. 1987) Hyper-Raman scattering by vibrational excitations in crystals, glasses and liquids. Phys Rep 151(1):1–92. 10.1016/0370-1573(87)90053-6
55. Coh S, Vanderbilt D (2022) Python Tight Binding (PythTB). Sep 20. 10.5281/zenodo.12721316. Zenodo
56. Kokalj A (Jun. 1999) XCrySDen—a new program for displaying crystalline structures and electron densities. J Mol Graph Model 17(3):176–179. 10.1016/S1093-3263(99)00028-5

# Figures

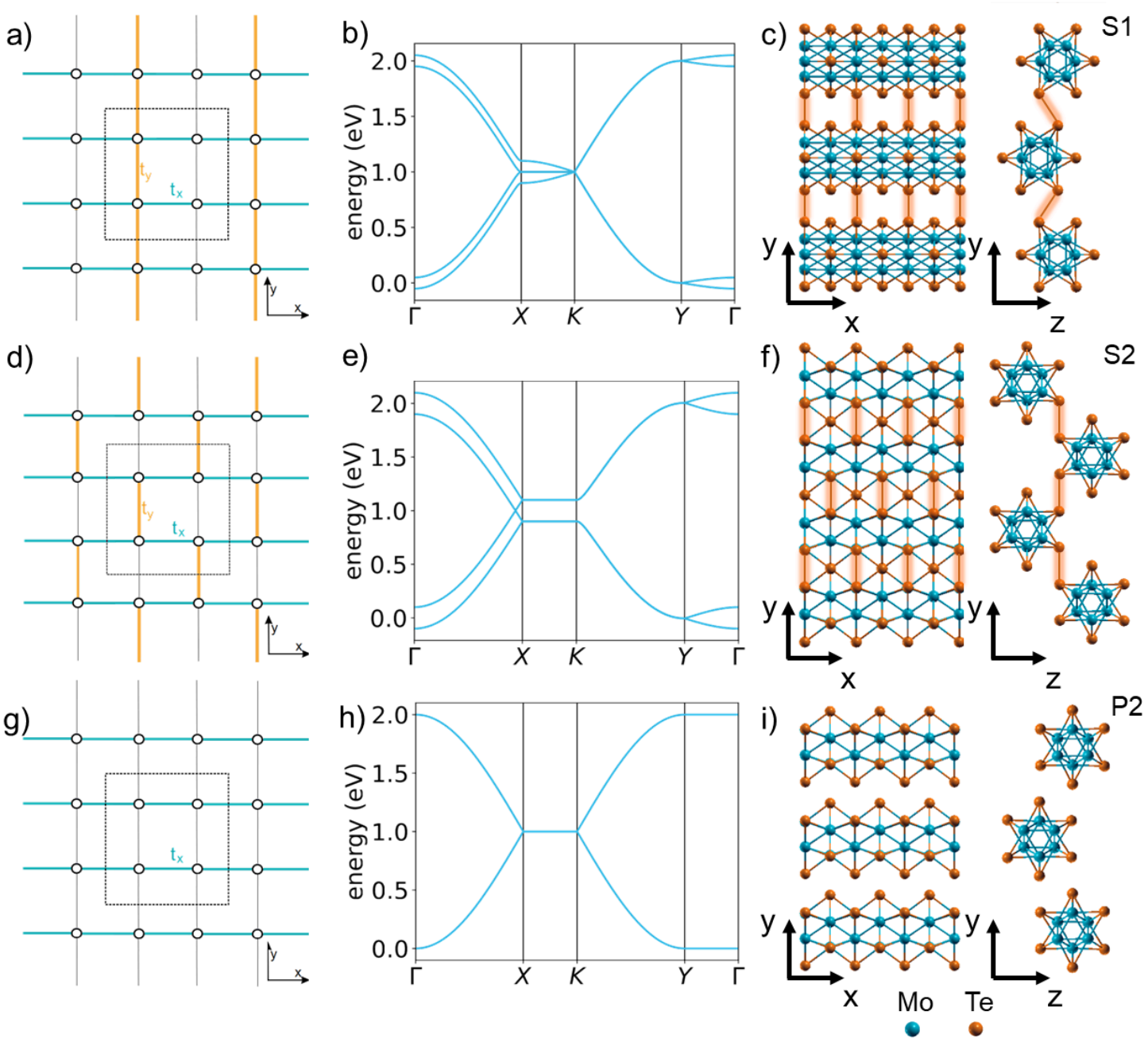


**Figure 1**

2D-SSH model representations, model band structures and monolayer 2D-$Mo_6Te_6$ ball-and-stick atomic structures. Panels (a, b, c): S1 phase. Panels (d, e, f): S2 phase. Panels (g, h, i): P2 phase

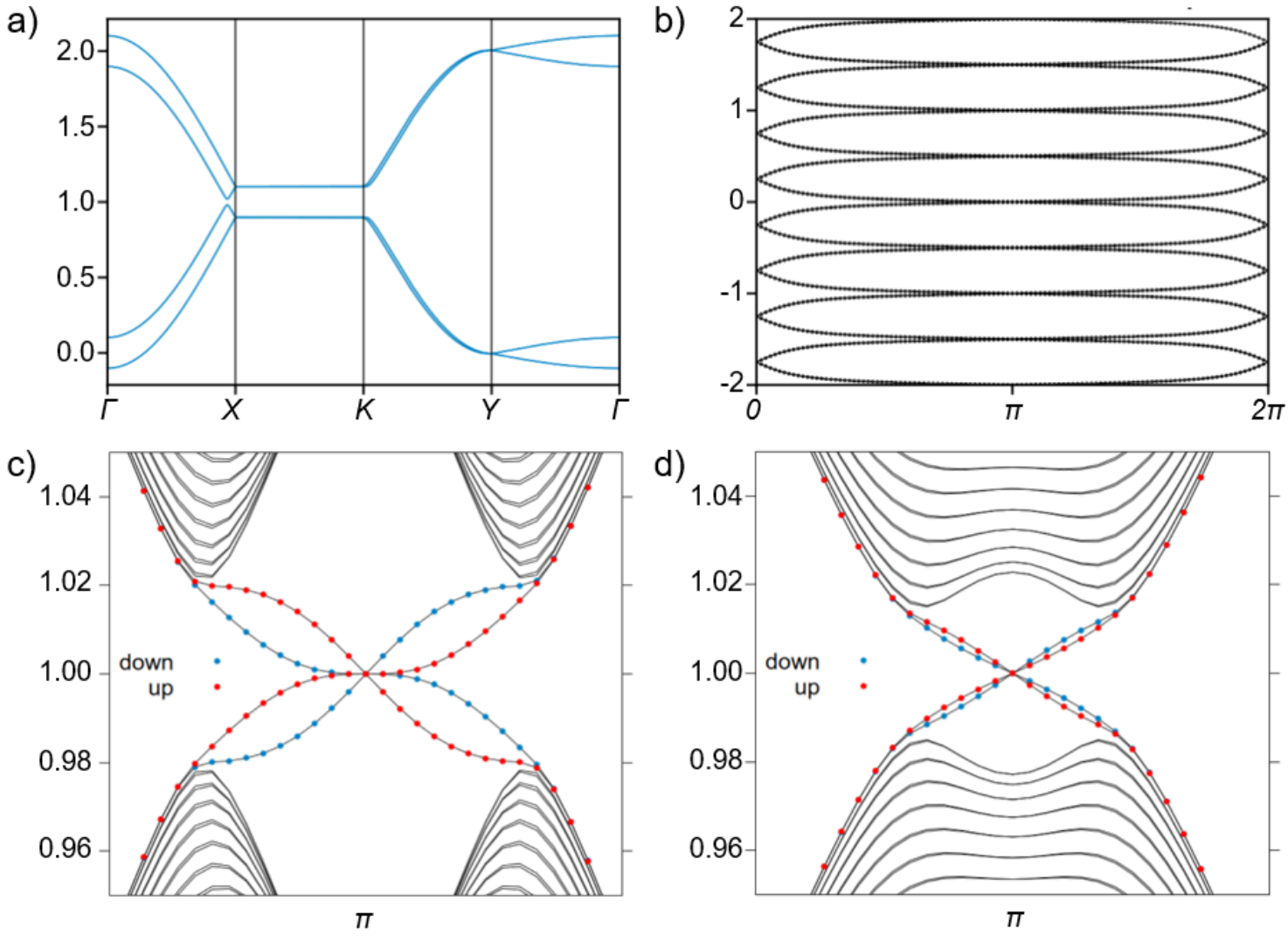


**Figure 2**

Band structure of the 2D-SSH model (S2 phase) with $t_x$ = 0.5 eV, $t_y$ = 0.1 eV and $\lambda_{SOC}$ = 0.01 eV. b) Hybrid Wannier centers behavior vs $k_x$. Helical edge states for the QSHI phase of the 2D-SSH model in a slab calculation with c) $n_y$ = 25, $t_x$ = 0.5 eV, $t_y$ = 0.1 eV and $\lambda_{SOC}$ = 0.01 eV and d) $n_y$ = 25, $t_x^{inter}$ = 0.54 eV, $t_x^{intra}$ = 0.46 eV, $t_y$ = 0.1 eV and $\lambda_{SOC}$ = 0.01 eV. Red and light blue point sizes are proportional to the spin up and down character of the state, respectively.

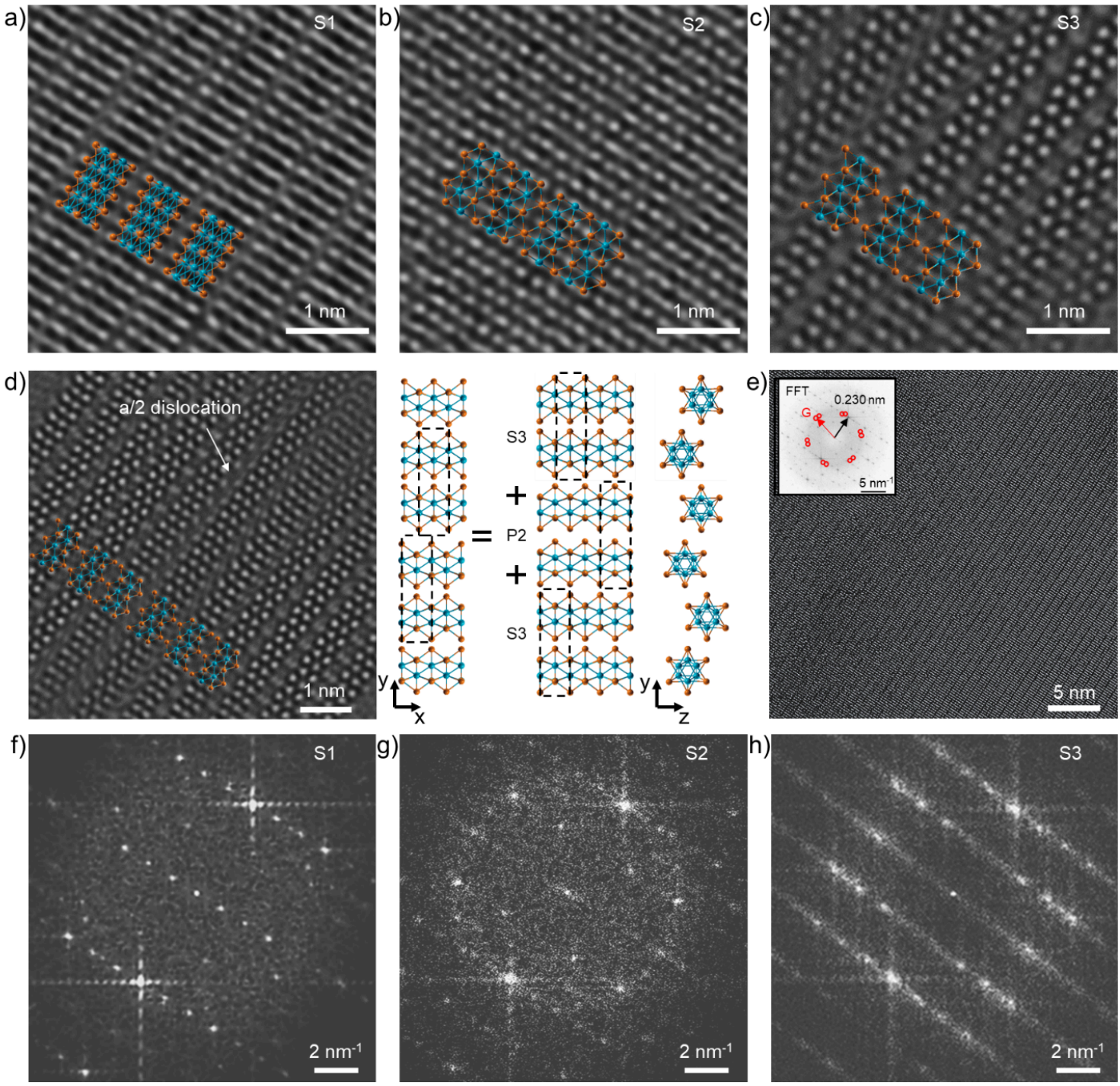


**Figure 3**

HRTEM characterization of monolayer 2D-$Mo_6Te_6$. (a-c) HRTEM images of three distinct in-plane lattice configurations observed in graphene-encapsulated 2D-$Mo_6Te_6$ after annealing, corresponding to the S1–S3 structural phases. Superimposed ball-and-stick models represent projected atomic structures derived from DFT and are consistent with the experimentally observed periodicities. (d) HRTEM image of a line defect within the S3 phase, corresponding to a relative lattice shift of approximately half a unit cell along the nanowire direction. (e) Larger-area HRTEM image of a continuous 2D-$Mo_6Te_6$ region and corresponding FFT. Diffraction spots from the $Mo_6Te_6$ lattice are distinguished from those of the

graphene encapsulation layer (marked as G), indicating high crystallinity and long-range ordering. (f–h) FFT patterns corresponding to the structures shown in panels (a–c), respectively. The distinct reciprocal-space features are consistent with the expected lattice symmetries and periodicities of the different phases.

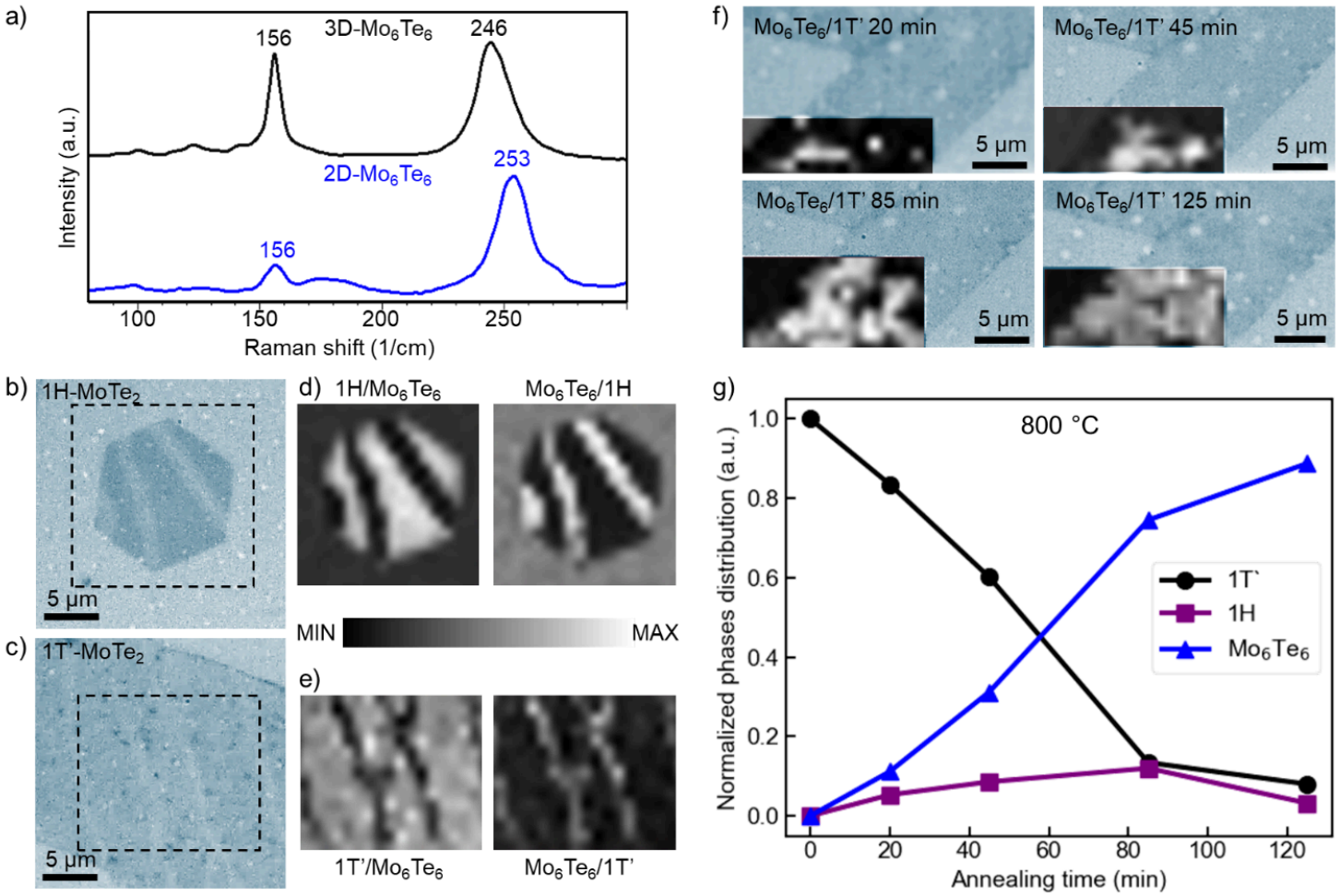


## Figure 4

(a) Raman spectra of 2D and 3D-$Mo_6Te_6$ detected after UHV annealing from monolayer and layered $MoTe_2$, respectively. Optical images of the 1H- and 1T'-$MoTe_2$. (b-c) optical micrographs of 1H and 1T'-$MoTe_2$ single crystals, respectively, encapsulated with defective graphene after annealing at 700°C for 60 minutes. The lighter optical contrast corresponds to $Mo_6Te_6$ regions as shown by the Raman maps in panels (d-e). We used the following Raman modes' intensities for mapping 1T'/$Mo_6Te_6$, $Mo_6Te_6$/1T', 1H/$Mo_6Te_6$ and $Mo_6Te_6$/1H relative spatial distributions shown in panels (d-e): 248-253 $cm^{-1}$ mode for $Mo_6Te_6$; $A_g^1$ mode at 84 $cm^{-1}$ for 1T'-$MoTe_2$; $E_{2g}$ mode at 235 $cm^{-1}$ for 1H-$MoTe_2$. (f) Raman maps of the 1T'-$MoTe_2$ to $Mo_6Te_6$ transformation at fixed 800 $^oC$ temperature after 20, 45 ,85 and 125 minutes of annealing. (g) Phases distribution as retrieved by Raman analyses after each annealing step, indicating simultaneous 1T' to 1H phase transformation in $MoTe_2$ as well as $Mo_6Te_6$ formation. The following

modes were used for Raman mapping: 248 or 254 $cm^{-1}$ modes for $Mo_6Te_6$, $A_g^1$ mode at 84 $cm^{-1}$ for 1T'-$MoTe_2$ and $E_{2g}$ mode at 235 $cm^{-1}$ for 1H-$MoTe_2$.

## Supplementary Files

This is a list of supplementary files associated with this preprint. Click to download.

- SIRealizationofaTunableTwodimensionalSuSchriefferHeegerModelinMonolayerMo6Te6.docx